

A Parameterization of the Cloud Scattering Polarization Signal Derived From GPM Observations for Microwave Fast Radiative Transfer Models

Victoria Sol Galligani^{1b}, Die Wang^{1b}, Paola Belén Corrales^{1b}, and Catherine Prigent^{1b}, *Member, IEEE*

Abstract—Microwave cloud polarized observations have shown the potential to improve precipitation retrievals since they are linked to the orientation and shape of ice habits. Stratiform clouds show larger brightness temperature (TB) polarization differences (PDs), defined as the vertically polarized TB (TBV) minus the horizontally polarized TB (TBH), with ~ 10 K PD values at 89 GHz due to the presence of horizontally aligned snowflakes, while convective regions show smaller PD signals, as graupel and/or hail in the updraft tend to become randomly oriented. The launch of the global precipitation measurement (GPM) microwave imager (GMI) has extended the availability of microwave polarized observations to higher frequencies (166 GHz) in the tropics and midlatitudes, previously only available up to 89 GHz. This study analyzes one year of GMI observations to explore further the previously reported stable relationship between the PD and the observed TBs at 89 and 166 GHz, respectively. The latitudinal and seasonal variability is analyzed to propose a cloud scattering polarization parameterization of the PD-TB relationship, capable of reconstructing the PD signal from simulated TBs. Given that operational radiative transfer (RT) models do not currently simulate the cloud polarized signals, this is an alternative and simple solution to exploit the large number of cloud polarized observations available. The atmospheric radiative transfer simulator (ARTS) is coupled with the weather research and forecasting (WRF) model, in order to apply the proposed parameterization to the RT simulated TBs and hence infer the corresponding PD values, which show to reproduce the observed GMI PDs well.

Index Terms—Clouds, microwave radiometry, passive microwave remote sensing.

Manuscript received September 9, 2020; revised December 2, 2020; accepted January 3, 2021. The work of Victoria Sol Galligani was supported by Proyectos de Investigación Científica y Tecnológica (PICT) under Grant 2016-0710. The work of Die Wang was supported by the United States (U.S.) Department of Energy (DOE) under Contract DE-SC0012704. (*Corresponding author: Victoria Sol Galligani.*)

Victoria Sol Galligani and Paola Belén Corrales are with the Centro de Investigaciones del Mar y la Atmósfera (CIMA, UBA-CONICET), Instituto Franco Argentino del Clima y sus Impactos (UMI3351-IFAEIC/CNRS-CONICET-UBA), Facultad de Ciencias Exactas y Naturales (FCEN-UBA), Buenos Aires 1428, Argentina (e-mail: victoria.galligani@cima.fcen.uba.ar).

Die Wang is with the Environmental and Climate Sciences Department, Brookhaven National Laboratory, Upton, NY 11973 USA.

Catherine Prigent is with LERMA, CNRS, PSL University, Sorbonne Université, Observatoire de Paris, F-75014 Paris, France.

Color versions of one or more figures in this article are available at <https://doi.org/10.1109/TGRS.2021.3049921>.

I. INTRODUCTION

AT LOW microwave frequencies (below 80 GHz), emission and absorption by the liquid phase in the clouds dominate satellite signals [1]. At higher frequencies (above 80 GHz), it is mainly ice particle scattering that drives the interaction between hydrometeors and the radiation that is received by passive microwave measurements [2]–[5]. Small pristine ice habits at high altitudes can also be more emissive than scattering, and as a result, their cold emission can be misinterpreted as scattering brightness temperature (TB) depressions. In most cases, the cloud scattering signal is determined largely by the microphysical properties of the ice particles (e.g., their composition, shape, orientation, and size distribution). However, a robust representation of the ice microphysical properties, especially their scattering properties, still remains a challenge in cloud-resolving and climate models, and radiative transfer (RT) simulations, due to the lack of observational constraints [6]–[8].

The scattering properties of ice particles can be calculated from several methods, such as the T-matrix method [9] or the discrete dipole approximation (DDA) [10]. There are several publicly available databases of DDA results for various particle shapes [11], [12], which have been used in many RT modeling studies. However, the ice particles in many retrievals and cloud-resolving models are assumed to be randomly oriented and to have simplified particle shapes and/or a constant density, which may induce large uncertainties [13]. Even if more complex and realistic ice particle shapes could be used, difficulties would still be encountered in choosing a single arbitrary shape that fits all observations (see [5], [6], [14]).

An important aspect of the passive microwave measurements is the TB polarization difference (PD), defined as the vertically polarized TB (TBV) minus the horizontally polarized TB (TBH). The PD has been used to identify convective and stratiform clouds and has shown potential to improve precipitation retrievals from satellite platforms, as previous studies have linked PD values to physical properties such as the orientation and shape of the ice phase (see [15]–[20]). However, current operational RT models are not capable of conducting cloud polarized simulations (e.g., the community radiative transfer model (CRTM) [21] or the radiative transfer

for TOVS (RTTOV) [22]), and increasing the complexity of the ice scattering calculations adds to the computational cost of the models, including nonoperational RT models (e.g., the atmospheric radiative transfer simulator (ARTS) [23]). For this reason, the present study aims at exploring alternative solutions capable of accounting for cloud polarized scattering in operational RT models.

A positive PD is observed at window microwave channels for cloudy cases (e.g., 89, 157, 243, and 640 GHz) due to the presence of horizontally oriented nonspherical ice hydrometeors [15]–[18], [24], [25]. A universal bell-curve relationship has been found between TBV and PD at these frequencies in cloudy regions, based on observations collected by both spaceborne [e.g., the Tropical Rainfall Measuring Mission (TRMM) Microwave Imager (TMI), the Microwave Analysis and Detection of Rain and Atmospheric Structures (MADRAS) instrument onboard Megha-Tropiques, and the global precipitation measurement (GPM) microwave imager (GMI)] and airborne [e.g., the International Sub-millimeter Airborne Radiometer (ISMAR), NASA’s Compact Scanning Submillimeter-wave Imaging Radiometer (CoSSIR)] passive microwave measurements that operate with conical scans in different climate regimes (see [17]–[19]). Conical scanners operate at constant incidence angle and fixed polarizations, whereas cross-track instruments scan across incidence angles and mix the polarization TBs. Currently, polarized TB observations are limited to 166 GHz (onboard GMI) and higher submillimeter frequencies are only available onboard ISMAR and COSSIR onboard demonstrator aircrafts. The upcoming conically scanning ice cloud imager (ICI) will measure both vertically and horizontally polarized at 243 and 664 onboard MetOp-SG (MetOp Second Generation) series of satellites.

In this study, we propose to parameterize the PD values as a function of the $TB = (TBV + TBH)/2$ [26]. To do so, we investigate one year of TB observations from Level-1C GMI [27] observations (2015) for precipitating clouds. Precipitation determination was obtained from GPM Level 2-A GPROF (Goddard Profiling) precipitation rainfall rate [28]. Different latitudinal parameterizations of the PD signals are built as a function of $TB = (TBV + TBH)/2$ for 89- and 166-GHz channels for land and ocean separately, based on the observed “bell-curve” relationship between PD and TB. The robustness of the proposed parameterization is assessed with respect to the sensitivity of the bell curve with seasons and latitude bands. Then, we evaluate the PD parameterization by comparing it with RT simulations for a mesoscale convective system (MCS) in Southeastern South America that is also observed by GMI. This case is simulated using the weather research and forecasting (WRF) [29] version 3.9.1, coupled with ARTS. The proposed parameterization is applied to the simulated TB to reconstruct the PD, which is then evaluated against the observed GMI PD values.

This article is structured as follows. Section II presents the data and the RT framework employed. In Section III, the bell curve observed by GMI from precipitating clouds over both land and ocean in 2015 is analyzed. Following a seasonal and latitudinal analysis, the PD-TB relationship is parameterized as a function of TB. Section IV evaluates the

proposed parameterization with a real case study observed with GMI, and Section V concludes this study.

II. OBSERVATIONAL DATA SET AND RT MODEL FRAMEWORK

A. GPM Observations

GMI onboard GPM flies at an altitude of 407 km in a non-Sun-synchronous orbit, scanning the Earth atmosphere with an off-nadir angle of 49° (53° incidence angle at the surface) between 68°S and 68°N [30]. It has swaths that are 885 km wide and 13 channels at 10.6, 18.7, 23.8, 36.5, 89, 166, 183.31 ± 3 , and 183.31 ± 7 GHz, where channels at 10.6, 18.7, 36.5, 89, and 166 GHz have both horizontal and vertical polarizations and all the other channels have only vertical polarization. The antenna-pattern polarization basis is aligned with the -v and -h basis at the Earth’s surface. In this study, we analyze one year of GMI Level-1C TBs [31] during 2015 primarily for the two window channels at 89 and 166 GHz. The footprint sizes for these two channels are of 7×4 km and 6×4 km, respectively. In addition, the GPM L2A GPROF algorithm [28] is used to map the rainfall characteristics of the analyzed TBs, mainly rainfall rate R . The GPROF R is used to discriminate the precipitating cloud PD signals from the surface PD signals observed by GMI under clear sky conditions. A rainfall rate threshold of $R > 1 \text{ mm h}^{-1}$ is used in this study to remove clear skies, shallow precipitating clouds, and nonprecipitating clouds.

B. RT Model Framework

To evaluate the proposed parameterization through RT simulations, we combine simulations from WRF [29] (version 3.9.1) and the ARTS RT model [23] (version 2.3). The WRF model is used to provide the atmospheric and surface conditions of the studied case to the RT model, including pressure, temperature, humidity, surface skin temperature, and the mixing ratios of the hydrometeors. The WRF simulations are performed with a 10-km horizontal grid spacing to match the GMI footprint sizes. WRF simulations are generated through a local ensemble transform Kalman filter (LETKF) [32] data assimilation and forecast system based on gridpoint statistical interpolation (GSI) using conventional observations from the WMO Binary Universal Form for Representation of Meteorological Data (BUFR) files processed at NCEP, an automatic stations regional network, and satellite-derived winds [33]. The following WRF parameterizations were used: YSU [34] for the planetary boundary layer, WSM6 [35] for microphysics, the modified version of the rapid RT model long-wave radiation [36], and the Dudhia short-wave radiation [37] schemes are employed, as well as the Noah Land Surface Model [38].

Regarding the RT simulations, the RT4 scattering solver [39] implemented inside ARTS is used to simulate the TBs together from the atmospheric and cloud variables provided by the WRF simulations described above. The RT4 model assumes plane-parallel geometry and employs the doubling-adding method, as do many operational RT models. The land surface emissivity used in the RT simulations is

derived from the Tool to Estimate Land Surface Emissivities from Microwave to Sub-millimeter waves model (TELSEM2) [40], which is used in other operational RT models (e.g., RTTOV) to provide realistic land surface emissivity values. Further details on the RT simulations performed are given in Section IV.

III. CHARACTERISTICS OF THE OBSERVED CLOUD POLARIZATION SIGNAL

A. Analysis of the GMI Observations

Fig. 1(a) and (b) shows the geographical distribution of the averaged PD at 166 GHz and the rainfall rate for the data analyzed (year 2015 and GPROF R above 1 mm h^{-1}). This is achieved by mapping all GMI observations and GPROF R onto a common $1^\circ \times 1^\circ$ grid. If multiple values of TB and/or R occurred in the same grid box, these were averaged. Fig. 1(c) shows the total number of precipitation events in each grid box. The highest rainfall rates and PD signals are found dominantly in the regions of the Inter Tropical Convergence Zone (ITCZ), jet regions, and frontal system passages in the midlatitudes (e.g., offshore of the east coast of North America), which is consistent with the global distribution of MCSs [41]. Fig. 1(a) shows a region of very large PD in Southeastern South America, where some of the most intense deep convective systems occur [42]–[45]. One intense MCS that developed on November 22, 2018 over this region is selected to evaluate the proposed PD parameterization (see Section IV). Note that deep convective cores that produce the strongest rainfall rates show weak PD signals in Fig. 1(a) as discussed in previous studies [16], [17], [25] due to the intense vertical air motion inside them that leads to nearly randomly oriented particles [41], [46]. Instead, the detrained stratiform clouds that are dominated by the aggregation of snow particles show relatively large PD values [47].

Fig. 1 shows the regions over the ocean at high latitudes with significant PD but weak R and a low number of precipitation events. This higher PD can be explained by the presence of sea ice, which has higher emissivities than open ocean surfaces and is additionally strongly polarized at 166 GHz [48]. The decrease in atmospheric opacity at higher latitudes also favors an increasing contribution of the surface polarization to the observed PD in these areas (see [49]). Removing GMI observations over sea ice, desert, snow surfaces, and water/land/ice boundaries, as determined by GPM surface flags, greatly reduces these high-latitude PD signals. For this reason, the following discussion excludes these GPM surface flags. Keeping in mind that in some cases, there is undetected sea ice by the GMI algorithm.

Fig. 2 shows the calculated median of the PD as a function of TB in different latitude bands for precipitating clouds observed by GMI with $R > 1 \text{ mm h}^{-1}$. In addition, we include in black the global PD median that includes all the available latitude bands (from 70°S to 70°N) and its corresponding standard deviation (SD). The medians are calculated with 2k bins for TB values and 1k bins for PD values. Fig. 2 shows that there is a clear distinction between the tropics and midlatitudes, and the land/ocean curves in the midlatitudes.

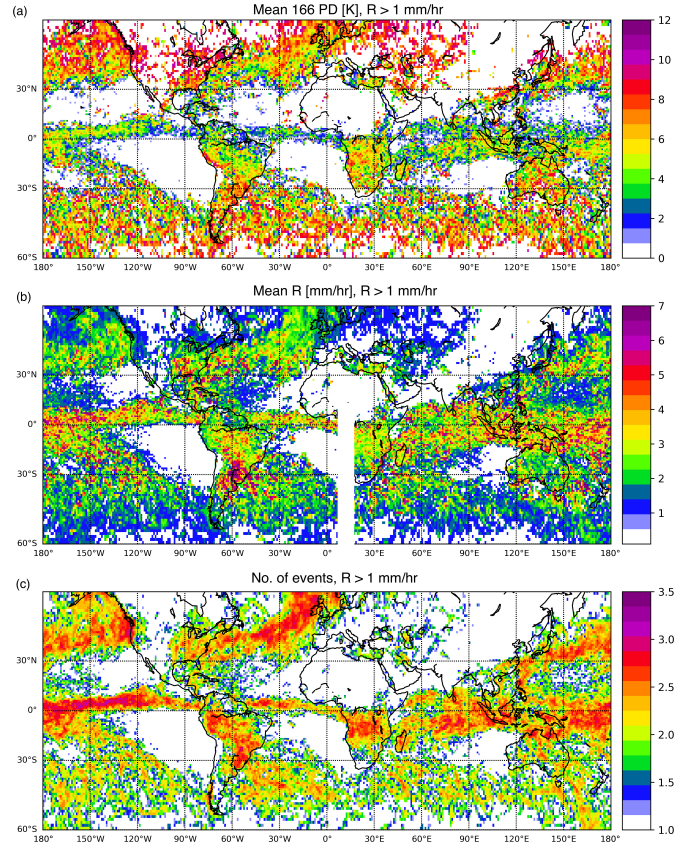


Fig. 1. (a) Mean PD (166 GHz) values for GMI data (2015) with $R > 1 \text{ mm h}^{-1}$. Additional information is provided in (b) regarding mean R and (c) number of events taken into account statistically with $R > 1 \text{ mm h}^{-1}$. The rainfall data were taken from the GPROF L2A GPM product.

Disregarding for now the highest latitudes (above $> \pm 50^\circ$), the PD peaks occur at about the same TB value for all latitude bands at 89 GHz ($\sim 220 \text{ K}$). The PD-TB behavior at low TB values (i.e., convective regions) is similar for all latitude bands. The weak polarization signals observed ($\text{PD} \sim 0 \text{ K}$) are a result of the presence of randomly oriented graupel and/or hail in strong convective updrafts. The PD tends to increase with latitude in both hemispheres, specially between 190 and 230 K for the 166-GHz channel, and this trend is stronger over the ocean than over land. This is consistent with results in previous studies [19], [25]. A lack of interhemispheric symmetry, discussed in [19], is shown for 166 GHz over land. In addition, all tropical bands between $\pm 30^\circ$ are shown to be similar. A distinct behavior is shown between oceanic and continental PD-TB relationships at 166 GHz, partially due to the strong diurnal variation of the PD over land at 166 GHz [19], [20] and due to much deeper convection occurring over land than over the ocean. In addition, as shown in [19], Fig. 2 shows that the increase in the PD with latitude is stronger over the ocean than over land. The variability in the PD-TB curves related to the latitude bands below $\pm 50^\circ$ is well within the SD of the global PD-TB curve. Note that the PD-TB curves show a very different behavior at the highest latitudes ($> |\pm 50^\circ|$), with large PD values, especially at 89 GHz over the ocean with PD values peaking at 20 K. This can be explained by the shallower clouds ($\text{TB} > \sim 200 \text{ K}$) that

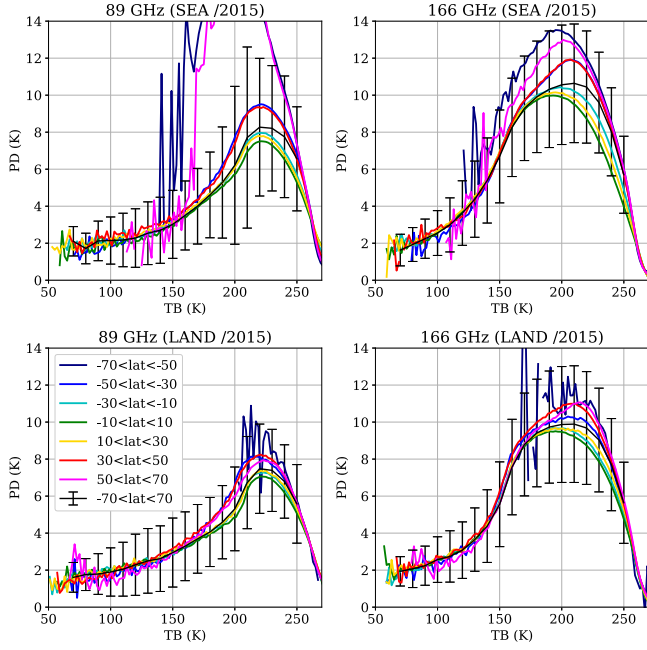


Fig. 2. PD median as a function of $TB = (TBV + TBH)/2$ for different latitude bands (see labels) for GMI data (2015). Only GMI data with GMI GPROF $R > 1 \text{ mm h}^{-1}$ is used to remove surface signals. (Top) Observations over the ocean at (a) 89 and (b) 166 GHz. (Bottom) Observations over land at (c) 89 and (d) 166 GHz. The black curve shows the global PD median taking into account all latitudes together (70°S – 70°N) and its error bars are derived from the SD. GMI observations over sea ice, desert, snow surfaces, and water/land/ice boundaries, as determined by GPM surface flags, are excluded from the data.

are relatively transparent at this frequency, and hence, the observed PD-TB curve includes the contribution from the highly polarized ocean surface. When eliminating the shallow clouds by increasing the rainfall R threshold to 3 mm h^{-1} , for example, we greatly limit the received surface emission and thus reduce the PD values for latitudes $> |\pm 50^\circ|$ by approximately 10 K at 89 GHz over the ocean.

Finally, the seasonal dependence of the PD-TB relationship is considered in Fig. 3 by analyzing the differences in the PD-TB parameterization for the entire year (solid lines) and the period comprising the months of December, January, February, and March (D, J, F, and M). This period comprises the wet (dry) season in the southern (northern) hemisphere. We find that the central tropical band between $10^\circ\text{S} < \text{latitude} < 10^\circ\text{N}$ (in green) shows no seasonal dependence, but in the tropical bands between 10° and 30° (in yellow), there is a very small variability of the PD-TB relationship ($< 1.5 \text{ K}$) for moderate TBs (175–240 K) as a result of the dry season in the northern hemisphere, higher at 166 GHz than 89 GHz. The opposite behavior occurs during June, July, August, and September (J, J, A, and S; not shown), where the small seasonal variability appears in the tropical bands between 30°S and 10°S . This seasonal variability in the 10° – 30° band of both hemispheres is as large as the land/ocean differences, well within the SD of the yearly curve. Note that the transition months are also analyzed (M, O, and N) and show a similar behavior as the yearly curve. Similarly, the seasonal variations of PD-TB relationship are analyzed for the midlatitudes for the northern hemisphere (30°N – 50°N , in red) and the southern

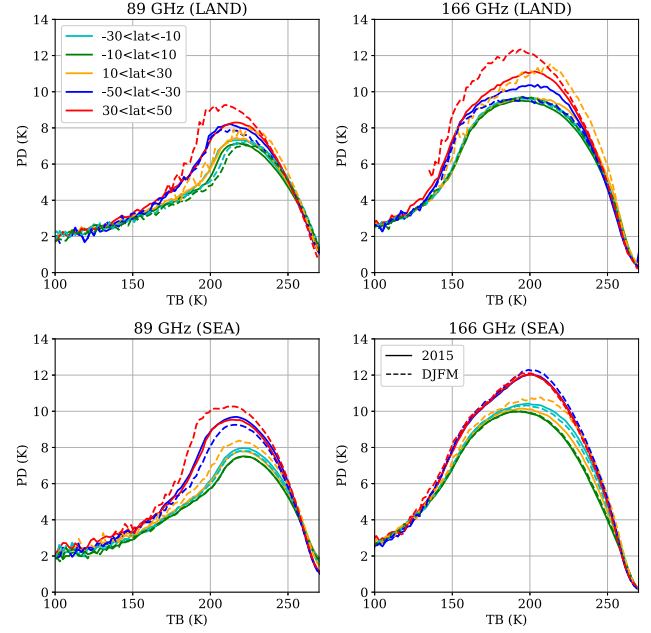


Fig. 3. PD median as a function of $TB = (TBV + TBH)/2$ for different latitude bands (see labels) for GMI data comprising 2015 (solid lines) and the period D, J, F, and M (dashed lines). Only GMI data with GMI GPROF $R > 1 \text{ mm h}^{-1}$ is used to remove surface signals. (Top) Observations over land at (a) 89 and (b) 166 GHz. (Bottom) Observations over sea at (c) 89 and (d) 166 GHz. GMI observations over sea ice, desert, snow surfaces, and water/land/ice boundaries, as determined by GPM surface flags, are excluded from the data.

hemisphere (30°S – 50°S , in blue). A seasonal dependence is also found for 89 GHz over both land and ocean, as well as for 166 GHz over land, for moderate TBs (175–240 K). The PD signal in the warm and wet season (i.e., in the southern hemisphere, blue line) is found to be lower than the one in the cold season (i.e., in the northern hemisphere, red line). A similar analysis for J, J, A, and S separately (not shown) throws similar conclusions. By comparing the PD-TB relationship for the warm/cold season in the northern/southern hemispheres (not shown), it can be concluded that at 89 GHz, the warm season PD-TB relationship is similar for the northern and the southern hemispheres over both land and sea, but at 166 GHz over land, these differences are not negligible ($\sim 1.5 \text{ K}$). As discussed previously regarding the latitudinal variations in Fig. 2, these seasonal variations are also within the SD around the yearly PD median. For this reason, the proposed parameterization does not consider the PD seasonal dependence.

B. Parameterization of the Observed Cloud PD Signal

From the discussion above, we aim to present three different parameterizations of the PD-TB median relationships shown in Fig. 4: one for the tropics (30°S – 30°N , in red), one for the midlatitudes (30° – 70° in both hemispheres, in blue), and a global parameterization (in black) at 89 and 166 GHz over the ocean and land separately. In addition, Fig. 4 shows the SDs for the three medians that are used as the error bars of the proposed parameterizations. The medians in Fig. 4 are calculated with 2k bins for TB values and 1k bins for PD values. The distinct behavior of the median midlatitudes

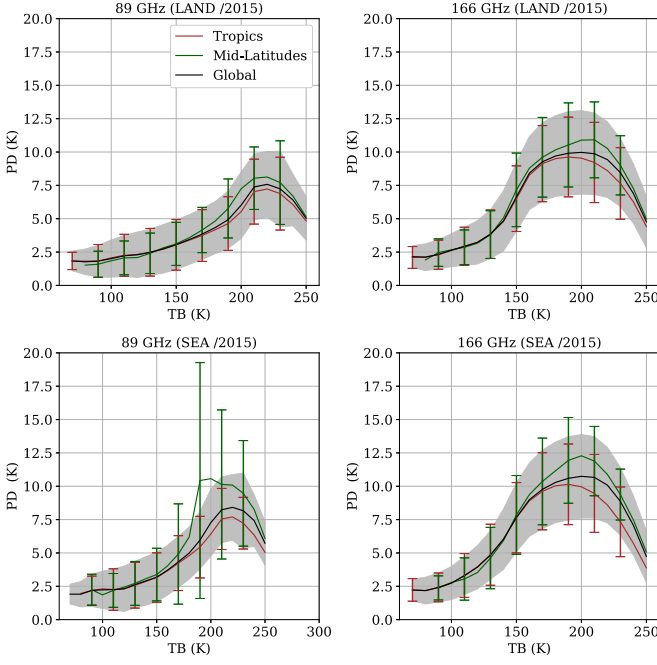


Fig. 4. PD median as a function of TB for the tropics, midlatitudes, and the global relationship (see labels) for GMI data (2015). Only GMI data with GMI GPROF $R > 1 \text{ mm h}^{-1}$ is used to remove surface signals. (Top) Observations over the ocean at (a) 89 and (b) 166 GHz. (Bottom) Observations over land at (c) 89 and (d) 166 GHz. The red and blue error bars are derived from the SD of the tropics and midlatitudes relationships, respectively, while the shaded gray area represents the SD around the global relationship. GMI observations over sea ice, desert, snow surfaces, and water/land/ice boundaries, as determined by GPM surface flags, are excluded from the data.

and tropical PD-TB curves motivates the proposal of these latitudinal parameterizations, in addition to the global parameterization, for regional applications.

The medians are parameterized using a cubic spline to build a lookup table of PD-TB pairs. Table I presents the proposed PD parameterization in 10k intervals as a function of TB (in the range 70–250 K) for 89 and 166 GHz for the global (black), tropics (red), and midlatitudes (blue) regions, over land and ocean surfaces. Note that only those bins in this 2015 data where the number of observations that fall into the tabulated PD-TB bins falls above 15 are considered. The median PD-TB curves can be reconstructed using this approach and the values remain inside one SD from the median curve (not shown).

IV. PARAMETERIZATION EVALUATION

A. Observations for a Case Study

An intense MCS over Southeastern South America observed by GMI is chosen to evaluate the proposed parameterizations. This event developed over central and northeastern Argentina during November 22, 2018 when a cold front crossed this region generating isolated convection that later grew into an MCS. Severe weather events were reported, and surface meteorological stations recorded values of 300 mm of accumulated precipitation. The available GMI PD observations at 37, 89, and 166 GHz are shown in Fig. 5 together with overlaid TBV contours at 180 K (in red) and 250 K (in magenta)

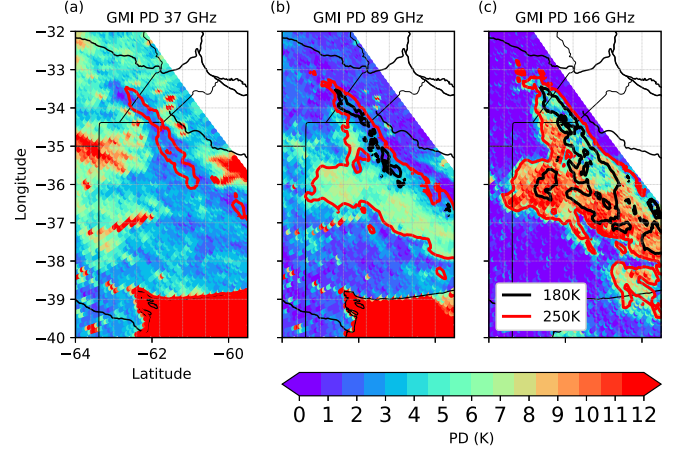


Fig. 5. GMI PD observations on November 22, 2018 at 0830 UTC over Argentina at (a) 37, (b) 89, and (c) 166 GHz. The red and magenta lines correspond to TBV contours at the TBs specified in the corresponding legends.

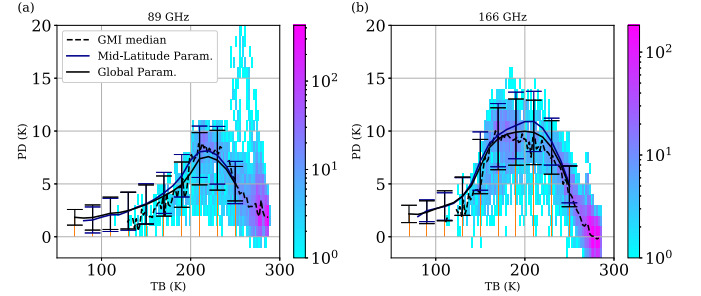


Fig. 6. PD-TB GMI median observed (dashed black lines) at (a) 89 and (b) 166 GHz over land for the domain of interest shown in Fig. 5. For each 1 K by 2 K PD-TB pair, the color indicates the normalized number of counts on a log scale. The blue and black solid lines, with their corresponding SDs as error bars, illustrate the proposed global and midlatitudes parameterizations.

for each channel. Note that Fig. 5 shows the TBV values rather than TB values as its accustomed in practice when analyzing GMI TBs. These TBV contours are illustrative of the regions of the lowest TB areas, which indicates the regions with the strongest convective cores. As expected, the coldest regions ($\text{TBV} < 180 \text{ K}$) show small PD values due to the stronger convective upward motion in convective cores. The stratiform areas ($180\text{--}250 \text{ K}$) show PD values that increase with frequency ($166 \text{ GHz PD} > 89 \text{ GHz PD} > 37 \text{ GHz PD}$). At 37 GHz, only the most intense convection is observed in TBV space (delimited by the 250 K TBV contour in red). Outside this contour, this frequency is less sensitive to the other areas of the MCS. The larger PD signals observed at 37 GHz (e.g., 15 K at 35°S and 64°W) mainly originate from the polarized surface. At 89 and 166 GHz, the contribution from the surface is limited, and the 180 K TBV contour area indicating the strongest convective regions shows low PD values, while the region within the 250 K contour shows a higher PD value that is associated with the stratiform regions of the system. Comparing the 37-GHz PD values in the geographical region delimited by the 89-GHz 250 TBV contour to the 89-GHz PDs further illustrates the sensitivity at 37 GHz to surface emission.

Fig. 6(a) and (b) shows the median PD-TB curve as calculated from the November 22, 2018 GMI observations shown

TABLE I
VECTOR OF INPUT TB NODES USED IN THE HERMITE SPLINE INTERPOLATION AND ITS CORRESPONDING PARAMETERIZED PD AT 89 AND 166 GHz OVER THE TROPICS IN RED, THE MID-LATITUDES IN BLUE, AND GLOBALLY IN BLACK OVER (A) LAND AND (B) OCEAN. THE CORRESPONDING SD FOR EACH PARAMETERIZATION IS ALSO INCLUDED

(a)

TB (K)	70	80	90	100	110	120	130	140	150	160	170	180	190	200	210	220	230	240	250
	PD (K)	PD (K)	PD (K)	PD (K)	PD (K)	PD (K)	PD (K)	PD (K)	PD (K)	PD (K)	PD (K)	PD (K)	PD (K)	PD (K)	PD (K)	PD (K)	PD (K)	PD (K)	PD (K)
89 GHz	1.84	1.82	1.84	2.01	2.26	2.32	2.49	2.71	3.04	3.39	3.74	4.17	4.64	5.53	7.03	7.23	6.89	6.04	4.83
	-	1.52	1.59	1.85	2.07	2.09	2.41	2.82	3.11	3.57	4.15	4.82	5.77	7.25	8.04	8.13	7.71	6.68	5.13
	1.84	1.77	1.82	2.01	2.22	2.29	2.48	2.74	3.05	3.44	3.85	4.33	4.93	6.02	7.38	7.58	7.24	6.39	5.02
166 GHz	0.65	0.96	1.23	1.43	1.57	1.75	1.79	1.89	1.90	1.92	1.94	1.94	2.01	2.36	2.43	2.32	2.73	1.99	2.00
	-	0.96	1.23	1.43	1.57	1.75	1.79	1.89	1.90	1.92	1.94	1.94	2.01	2.36	2.43	2.32	2.73	1.99	2.00
	0.74	0.95	1.19	1.39	1.53	1.70	1.74	1.81	1.85	1.86	1.90	1.95	2.14	2.50	2.47	2.46	2.83	1.92	1.63
166 GHz	2.16	2.12	2.32	2.64	2.93	3.23	3.84	4.83	6.64	8.42	9.27	9.70	9.90	9.98	9.87	9.43	8.45	6.89	4.76
	-	1.91	2.46	2.67	2.86	3.16	3.80	5.06	7.16	8.80	9.61	10.16	10.53	10.89	10.91	10.27	9.00	7.26	4.97
	2.16	2.12	2.32	2.64	2.93	3.23	3.84	4.83	6.64	8.42	9.27	9.70	9.90	9.98	9.87	9.43	8.45	6.89	4.76
166 GHz	0.82	1.00	1.09	1.25	1.43	1.65	1.81	2.16	2.46	2.69	2.85	2.91	2.99	3.01	3.01	2.88	2.68	2.40	2.06
	-	0.97	1.03	1.10	1.30	1.44	1.79	2.56	2.76	2.80	2.99	3.09	3.15	3.06	2.85	2.54	2.22	1.95	1.76
	0.82	1.00	1.08	1.24	1.42	1.62	1.81	2.26	2.57	2.75	2.93	3.02	3.13	3.13	3.05	2.83	2.53	2.22	1.92

(b)

TB (K)	70	80	90	100	110	120	130	140	150	160	170	180	190	200	210	220	230	240	250
	PD (K)	PD (K)	PD (K)	PD (K)	PD (K)	PD (K)	PD (K)	PD (K)	PD (K)	PD (K)	PD (K)	PD (K)	PD (K)	PD (K)	PD (K)	PD (K)	PD (K)	PD (K)	PD (K)
89 GHz	-	1.97	2.17	2.31	2.25	2.31	2.58	2.86	3.15	3.66	4.24	4.80	5.44	6.42	7.55	7.70	7.23	6.34	5.04
	-	-	2.24	1.86	2.19	2.44	2.72	3.07	3.38	4.03	4.92	6.20	10.43	10.57	10.14	10.09	9.47	8.26	6.09
	1.91	1.91	2.20	2.23	2.25	2.32	2.63	2.9	3.19	3.71	4.33	4.99	5.96	7.27	8.24	8.42	8.16	7.43	5.73
166 GHz	-	0.99	1.09	1.34	1.56	1.61	1.71	1.86	1.86	1.94	2.06	2.19	2.31	2.44	2.30	2.13	1.94	1.73	1.68
	-	-	1.09	1.34	1.56	1.61	1.71	1.86	1.86	1.94	2.06	2.20	2.31	2.44	2.29	2.13	1.94	1.73	1.68
	0.72	0.93	1.10	1.28	1.53	1.58	1.70	1.83	1.89	2.00	2.42	3.57	5.96	5.61	4.38	3.93	3.60	2.99	2.21
166 GHz	2.22	2.18	2.41	2.74	3.30	3.93	4.84	6.03	7.67	9.00	9.77	10.29	10.60	10.75	10.67	10.08	8.86	7.07	4.73
	-	-	2.38	2.78	3.04	3.53	4.62	5.92	7.85	9.38	10.36	11.15	11.94	12.28	11.88	10.88	9.38	7.47	5.07
	2.22	2.18	2.41	2.74	3.30	3.94	4.84	6.03	7.67	9.00	9.77	10.29	10.60	10.75	10.67	10.08	8.86	7.07	4.73
166 GHz	0.85	0.98	1.08	1.36	1.64	1.97	2.29	2.53	2.64	2.75	2.89	2.97	3.02	3.00	2.92	2.80	2.61	2.35	1.94
	-	-	0.90	1.07	1.59	1.72	2.30	2.87	2.95	3.15	3.25	3.30	3.21	2.96	2.60	2.24	1.91	1.69	1.56
	0.85	0.99	1.07	1.34	1.64	1.96	2.30	2.57	2.69	2.84	3.02	3.14	3.23	3.20	3.03	2.76	2.41	2.09	1.79

in Fig. 5 for 89 and 166 GHz over land (black dashed lines), respectively. Similar to the analysis shown in Section III, for each 1 K by 2 K PD-TB box, the color in Fig. 6 indicates the normalized number of counts in each PD-TB pair on a log scale for the observations shown in Fig. 5. The black and blue solid lines and their error bars illustrate the proposed global and midlatitudes parameterizations presented in Table I, respectively. The parameterizations agree well with the PD-TB relationship for this particular case, and differences are within the PD-TB SD. For the lower end of TB values, the parameterization slightly overestimates PD at 89 and 166 GHz. For the higher TB values at 89 GHz, between 250 and 300 K, the large PD values shown that yield a clear lambda shape correspond to the few pixels in Fig. 5 over the sea.

B. Parameterization Evaluation Through RT

In this section, we evaluate the proposed parameterization through RT simulations, as described in Section II-B. The aim is to reconstruct the PD signal from the simulated TB. We simulate the case study in Fig. 5 using WRF+ARTS(RT4) to test the performance of the proposed midlatitude parameterization. Similar results are found when employing the global parameterization (not shown).

The WRF-WSM6 scheme predicts five hydrometeor categories: cloud liquid, cloud ice, rain, snow, and graupel. The single-scattering properties of cloud water and cloud ice are calculated as randomly oriented spheres following Mie theory, using the dielectric properties following Liebe *et al.* [50] for liquid species and Mätzler [51] for cloud ice. These are reasonable assumptions for the liquid phase and pristine ice habits in these microwave frequencies. The single-scattering properties of raindrops are calculated using the T-matrix approach assuming randomly oriented spheres. Finally, the single-scattering properties of snow and graupel species are derived from the Liu (2008) DDA data set [11] for randomly oriented sector habits. This is known as the “one-size-fits-all” sector snowflake model following Geer and Baordo [8], which is currently employed in RTTOV-SCATT operational setup. For all the hydrometeor types considered in the RT simulations, their corresponding WRF-WSM6 gamma particle size distributions (PSDs) of the form $N_x(D) = \int N_{0x} D^{\mu_x} \exp(-\lambda_x D) dD$ are used, where $N_x(D)$ represents the number concentration of particles of a given hydrometeor class (x , i.e., snow, rain, cloud, graupel, and ice) and diameter D , N_{0x} is the y intercept parameter, μ_x represents the slope parameter, and λ_x is the shape parameter of the distribution. Exploring the impact of the PSD on simulated TB is outside the scope of the present work. In order to apply the optical properties of the Liu (2008) DDA database to the WRF(WSM6) snowflakes consistently, the equal mass approach is introduced [5]. The equal mass approach consists of describing the optical properties of the WRF snowflakes with the optical properties of habits in the DDA database whose dimensions might be different (D') but whose mass is conserved through $a_{\text{WRF}} D'^{b_{\text{WRF}}} = a_{\text{DDA}} D'^{b_{\text{DDA}}}$, where a_{WRF} (a_{DDA}) and b_{WRF} (b_{DDA}) are the parameters of the mass-size relationship of WRF-WSM6 (intrinsic to the DDA Sector habit).

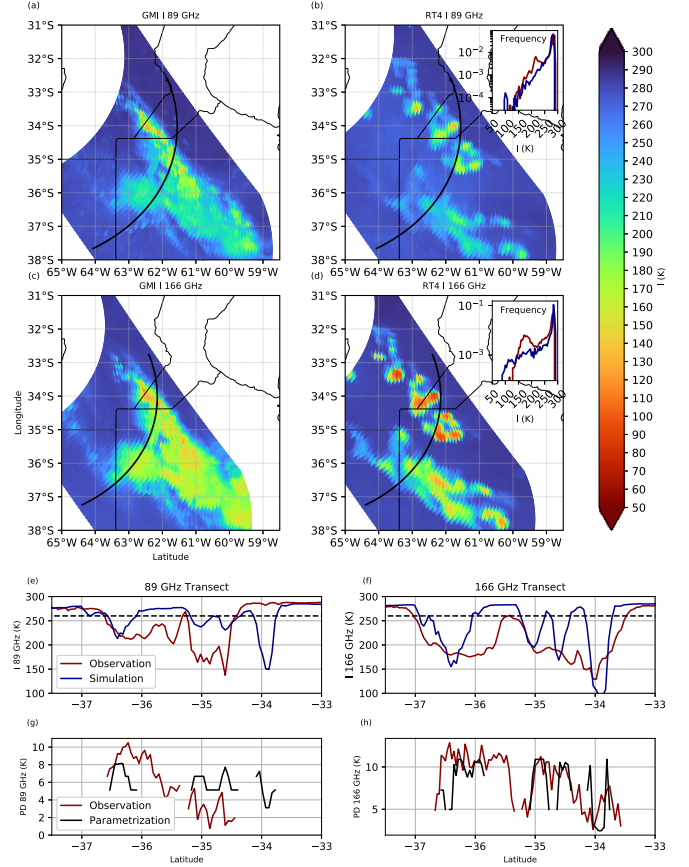


Fig. 7. (a) and (c) Observed GMI TB values on November 22, 2018 at 08:30 UTC for the region of interest at 89 and 166 GHz, respectively. (b) and (d) Corresponding WRF+ARTS(RT4) simulations at 89 and 166 GHz, respectively. [Top-right corner of (b) and (d)] Frequency distribution of the simulated (blue line) and observed (red line) TB values, using 5k bins at 89 and 166 GHz, respectively. The black line overlaid in all first four figures illustrates a specific GMI transect analyzed in detail in (e)–(f), where the observed and simulated TB values are shown as georeferenced with latitude. (g)–(h) Observed and reconstructed PD values through the proposed midlatitude parameterizations over land.

ARTS(RT4) is run to compute $TB = (TBV + TBH)/2$ from which to reconstruct the observed PD at 89 and 166 GHz using the proposed midlatitude parameterization.

Fig. 7 shows the observed TB from GMI at 89 GHz of the selected MCS case study on the top left [see Fig. 7(a)] and the corresponding RT4 simulations on the top right [see Fig. 7(b)]. The TBs agree well between the GMI observations and the RT4 simulations at 89 GHz. Similarly, Fig. 7(c) and (d) shows the TB observations and simulations at 166 GHz, respectively. When comparing the simulations with the observations, it is important to remember that the RT simulations depend mainly on: 1) the integrated species content modeled by WRF; 2) the WRF microphysics parameterization; and 3) the assumed single-scattering properties, especially for the snowflakes and graupel. For example, Fig. 7(c) and (d) shows that the simulated TB at 166 GHz is colder than observed. Either WRF generates more scattering species than actually present at the time of the GPM passage or the RT model (and its necessary assumptions) simulates excessive scattering or both. The WRF-WSM6 is known to generate excessive

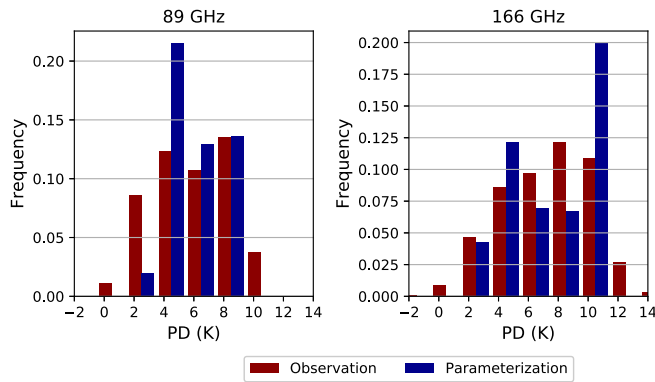


Fig. 8. Statistical distribution of the observed PD values (red line) and the reconstructed PD values (blue line) using RT simulations and the proposed midlatitude parametrization at (a) 89 and (b) 166 GHz.

graupel species [5], which could induce an overestimation of the scattering signals.

It is important to show that the simulated TB values are comparable to the observed values since the proposed parameterization is to be applied to the simulated TB. To analyze the representativeness of the RT simulations, the top-right corner of Fig. 7(b) and (d) shows the frequency distribution of the simulated (blue line) and observed (red line) TB values, using 5k bins. The 89-GHz simulations are shown to perform well. The differences are larger at 166 GHz than at 89 GHz, with simulated TB values lower than the observations and an underestimation of simulated values between 140 and 220 K. The χ^2 test of these distributions was evaluated as a measure of how close the simulated distributions are to the observed distributions. The χ^2 test follows from $\chi^2 = \sum E_i$, where $E_i = [X(i) - Y(i)] / (X(i))^{1/2}$. $X(i)$ and $Y(i)$ are the relative frequencies of the observations and the simulations in the respectively computed i th bins. The χ^2 test of these distributions, considering only bins below 260 K in order to neglect clear-sky pixels and focus on the cloudy contribution over land, shows good consistency in a statistical sense with values of 0.14 and 0.27 at 89 and 166 GHz, respectively. In the next step, the parameterization is applied to the simulated TB values to reconstruct the observed PDs and compare it with the observations. Fig. 7(e)–(h) shows the observed and simulated TB and PD values along a specific transect (shown by the black lines in Fig. 7) at 89 and 166 GHz. As expected, the TB depressions associated with ice cloud scattering are not simulated at the exact latitude as actually observed, since WRF has uncertainties in capturing the MCS passage [52]. Fig. 7(g) shows the observed PD in black and the reconstructed PD using the midlatitude parameterization proposed in red at 89 GHz. Similarly, Fig. 7(h) shows the same comparison at 166 GHz. The parameterization is shown to well represent the observed PD. Fig. 8 shows the statistical distribution of the observed PD values at 89 and 166 GHz together with the reconstructed PD values using the proposed parameterization.

V. SUMMARY

Previous studies have shown that stratiform clouds have large microwave polarized signals PD values of the order

of 10 K at 89 and 166 GHz) due to the presence of horizontally aligned large ice and mixed-phase hydrometeors. In contrast, convective regions show weak polarization signals (close to 0 K) and have low TBs due to the presence of randomly oriented graupel and/or hail in strong turbulent updrafts. Polarized microwave cloud scattering signals have been shown to have a robust PD-TB bell-curve type relation. The present study analyzes one year of GMI Level 1C TB observations and this bell curve. Larger PDs are found at 166 GHz than at 89 GHz, due to the scattering properties of the ice phase increasing with frequency. The regional and seasonal variability of the bell curve is analyzed and different parameterizations are derived using hermite cubic spline interpolation for global/tropics/midlatitudes regions for land/ocean surfaces at 89 and 166 GHz. Robust parameterizations allow the reconstruction of the PD signal from simulated TBs with fast RT simulations. This is important, given that operational RT models do not currently simulate the cloud polarized signal and that significant to large PD signals have been observed for large frequencies above 80 GHz. The suggested parameterizations will make it possible to simulate the cloud polarized signal measured by the current satellites, from fast RT models. An RT modeling framework is applied to an observed MCS in South Eastern South America to evaluate the proposed parameterization. The proposed parameterization is used together with a plane-parallel fast RT model to simulate randomly oriented DDA Liu (2008) sector habits and is shown to reproduce the observed polarization successfully. This parameterization has the potential to be used operationally in fast RT simulation and exploit the large number of cloud polarized observations available. Future work will compare these results with the recently available ARTS DDA scattering database [12] that includes ice habits with horizontally aligned orientations. However, even if more complex and realistic ice particle shapes could be used, a fully polarized sophisticated ice-scattering calculation is very computational expensive and time consuming. Future work will also focus on exploring and extending this work to PD signals at higher submillimeter frequencies. This is important in the context of the upcoming conically scanning radiometer ICI, which will measure both vertical and horizontal polarizations at 243 and 664 GHz onboard the MetOp-SG operational European satellite.

ACKNOWLEDGMENT

The publisher by accepting the article for publication acknowledges that the United States Government retains a nonexclusive, paid-up, irrevocable, worldwide license to publish or reproduce the published form of this article, or allow others to do so, for United States Government purposes.

REFERENCES

- [1] C. Kummerow and J. A. Weinman, "Determining microwave brightness temperatures from precipitating horizontally finite and vertically structured clouds," *J. Geophys. Res., Atmos.*, vol. 93, pp. 3720–3728, Apr. 1988.
- [2] G. M. Skofronick-Jackson, M.-J. Kim, J. A. Weinman, and D.-E. Chang, "A physical model to determine snowfall over land by microwave radiometry," *IEEE Trans. Geosci. Remote Sens.*, vol. 42, no. 5, pp. 1047–1058, May 2004.

- [3] R. Bennartz and P. Bauer, "Sensitivity of microwave radiances at 85–183 GHz to precipitating ice particles," *Radio Sci.*, vol. 38, no. 4, pp. 40-1–40-8, Aug. 2003.
- [4] D. Wang, C. Prigent, F. Aires, and C. Jimenez, "A statistical retrieval of cloud parameters for the millimeter wave ice cloud imager on board MetOp-SG," *IEEE Access*, vol. 5, pp. 4057–4076, 2017.
- [5] V. S. Galligani, D. Wang, M. A. Imaz, P. Salio, and C. Prigent, "Analysis and evaluation of WRF microphysical schemes for deep moist convection over South-Eastern South America (SESA) using microwave satellite observations and radiative transfer simulations," *Atmos. Meas. Techn.*, vol. 10, no. 10, pp. 3627–3649, Oct. 2017.
- [6] M. S. Kulie, R. Bennartz, T. J. Greenwald, Y. Chen, and F. Weng, "Uncertainties in microwave properties of frozen precipitation: Implications for remote sensing and data assimilation," *J. Atmos. Sci.*, vol. 67, no. 11, pp. 3471–3487, Nov. 2010.
- [7] B. T. Johnson, G. W. Petty, and G. Skofronick-Jackson, "Microwave properties of ice-phase hydrometeors for radar and radiometers: Sensitivity to model assumptions," *J. Appl. Meteorol. Climatol.*, vol. 51, no. 12, pp. 2152–2171, Dec. 2012.
- [8] A. J. Geer and F. Baordo, "Improved scattering radiative transfer for frozen hydrometeors at microwave frequencies," *Atmos. Meas. Techn.*, vol. 7, no. 6, pp. 1839–1860, Jun. 2014.
- [9] M. I. Mishchenko, L. D. Travis, and D. W. Mackowski, "T-matrix computations of light scattering by nonspherical particles: A review," *J. Quant. Spectrosc. Radiat. Transf.*, vol. 55, no. 5, pp. 535–575, May 1996.
- [10] B. T. Draine and P. J. Flatau, "Discrete-dipole approximation for scattering calculations," *J. Opt. Soc. Amer. A, Opt. Image Sci.*, vol. 11, no. 4, pp. 1491–1499, 1994.
- [11] G. Liu, "A database of microwave single-scattering properties for nonspherical ice particles," *Bull. Amer. Meteorol. Soc.*, vol. 89, no. 10, pp. 1563–1570, Oct. 2008.
- [12] P. Eriksson, R. Ekelund, J. Mendrok, M. Brath, O. Lemke, and S. A. Buehler, "A general database of hydrometeor single scattering properties at microwave and sub-millimetre wavelengths," *Earth Syst. Sci. Data*, vol. 10, no. 3, pp. 1301–1326, Jul. 2018.
- [13] C. D. Kummerow *et al.*, "The evolution of the goddard profiling algorithm to a fully parametric scheme," *J. Atmos. Ocean. Technol.*, vol. 32, no. 12, pp. 2265–2280, Dec. 2015.
- [14] V. S. Galligani *et al.*, "Meso-scale modelling and radiative transfer simulations of a snowfall event over france at microwaves for passive and active modes and evaluation with satellite observations," *Atmos. Meas. Techn.*, vol. 8, no. 3, pp. 1605–1616, Mar. 2015.
- [15] C. Prigent, E. Matthews, F. Aires, and W. B. Rossow, "Remote sensing of global wetland dynamics with multiple satellite data sets," *Geophys. Res. Lett.*, vol. 28, no. 24, pp. 4631–4634, Dec. 2001.
- [16] C. Prigent, E. Defer, J. R. Pardo, C. Pearl, W. B. Rossow, and J.-P. Pinty, "Relations of polarized scattering signatures observed by the TRMM microwave instrument with electrical processes in cloud systems," *Geophys. Res. Lett.*, vol. 32, no. 4, Feb. 2005, Art. no. L04810.
- [17] V. S. Galligani, C. Prigent, E. Defer, C. Jimenez, and P. Eriksson, "The impact of the melting layer on the passive microwave cloud scattering signal observed from satellites: A study using TRMM microwave passive and active measurements," *J. Geophys. Res., Atmos.*, vol. 118, no. 11, pp. 5667–5678, Jun. 2013.
- [18] E. Defer, V. S. Galligani, C. Prigent, and C. Jimenez, "First observations of polarized scattering over ice clouds at close-to-millimeter wavelengths (157 GHz) with MADRAS on board the Megha-Tropiques mission," *J. Geophys. Res., Atmos.*, vol. 119, no. 21, pp. 301–316, 2014.
- [19] J. Gong and D. L. Wu, "Microphysical properties of frozen particles inferred from global precipitation measurement (GPM) microwave imager (GMI) polarimetric measurements," *Atmos. Chem. Phys.*, vol. 17, no. 4, pp. 2741–2757, Feb. 2017.
- [20] X. Zeng, G. Skofronick-Jackson, L. Tian, A. E. Emory, W. S. Olson, and R. A. Kroodsma, "Analysis of the global microwave polarization data of clouds," *J. Climate*, vol. 32, no. 1, pp. 3–13, Jan. 2019.
- [21] Q. Liu and F. Weng, "Advanced doubling-adding method for radiative transfer in planetary atmospheres," *J. Atmos. Sci.*, vol. 63, no. 12, pp. 3459–3465, Dec. 2006.
- [22] R. Saunders *et al.*, "An update on the RTTOV fast radiative transfer model (currently at version 12)," *Geosci. Model Develop.*, vol. 11, no. 7, pp. 2717–2737, Jul. 2018.
- [23] P. Eriksson, S. A. Buehler, C. P. Davis, C. Emde, and O. Lemke, "ARTS, the atmospheric radiative transfer simulator, version 2," *J. Quant. Spectrosc. Radiat. Transf.*, vol. 112, no. 10, pp. 1551–1558, Jul. 2011.
- [24] R. W. Spencer, H. M. Goodman, and R. E. Hood, "Precipitation retrieval over land and ocean with the SSM/I: Identification and characteristics of the scattering signal," *J. Atmos. Ocean. Technol.*, vol. 6, no. 2, pp. 254–273, Apr. 1989.
- [25] J. Gong *et al.*, "Linkage among ice crystal microphysics, mesoscale dynamics, and cloud and precipitation structures revealed by collocated microwave radiometer and multifrequency radar observations," *Atmos. Chem. Phys. Discuss.*, vol. 20, no. 21, pp. 1–32, 2020.
- [26] V. Galligani, D. Wang, and C. Prigent, "Poster: Microphysical properties of ice and mixed-phase cloud particles as revealed by GPM microwave polarimetric measurements and radiative transfer modeling," in *Proc. Amer. Geophys. Union (AGU) Fall Meeting*, Dec. 2019.
- [27] W. Berg, "GPM GMI common calibrated brightness temperatures collocated L1C 1.5 hours 13 km V05," Goddard Earth Sci. Data Inf. Services Center (GES DISC), Greenbelt, MD, USA, Tech. Rep., 2016.
- [28] T. Iguchi and R. Meneghini, "GPM GMI (GPROF) radiometer precipitation profiling L2A 1.5 hours 13 km V05," Goddard Earth Sci. Data Inf. Services Center (GES DISC), Greenbelt, MD, USA, Tech. Rep., 2016.
- [29] W. C. Skamarock and Coauthors, "A description of the advanced research WRF version 3," Nat. Center Atmos. Res., Boulder, CO, USA, NCAR Tech. Rep. NCAR/TN-475+STR, 2008, doi: [10.5065/D68S4MVH](https://doi.org/10.5065/D68S4MVH).
- [30] G. Skofronick-Jackson *et al.*, "The Global Precipitation Measurement (GPM) mission for science and society," *Bull. Amer. Meteorol. Soc.*, vol. 98, pp. 1679–1695, Aug. 2017.
- [31] Z. Liu *et al.*, "Global precipitation measurement mission products and services at the NASA GES DISC," *Bull. Amer. Meteorol. Soc.*, vol. 98, no. 3, pp. 437–444, Mar. 2017.
- [32] B. R. Hunt, E. J. Kostelich, and I. Szunyogh, "Efficient data assimilation for spatiotemporal chaos: A local ensemble transform Kalman filter," *Phys. D, Nonlinear Phenomena*, vol. 230, nos. 1–2, pp. 112–126, Jun. 2007.
- [33] P. Corrales *et al.*, "Assimilation of conventional observations in a deep convection case during RELAMPAGO using the WRF-GSI-LETKF system," in *Proc. RELAMPAGO DAW*, Buenos Aires, Argentina, Nov. 2019, pp. 19–22.
- [34] S.-Y. Hong, Y. Noh, and J. Dudhia, "A new vertical diffusion package with an explicit treatment of entrainment processes," *Monthly Weather Rev.*, vol. 134, no. 9, pp. 2318–2341, Sep. 2006.
- [35] S.-Y. Hong and J.-O. J. Lim, "The WRF single-moment 6-class microphysics scheme (WSM6)," *J. Korean Meteorol. Soc.*, vol. 42, no. 2, pp. 129–151, 2006.
- [36] E. J. Mlawer, S. J. Taubman, P. D. Brown, M. J. Iacono, and S. A. Clough, "Radiative transfer for inhomogeneous atmospheres: RRTM, a validated correlated-k model for the longwave," *J. Geophys. Res., Atmos.*, vol. 102, no. D14, pp. 16663–16682, 1997.
- [37] J. Dudhia, "Numerical study of convection observed during the winter monsoon experiment using a mesoscale two-dimensional model," *J. Atmos. Sci.*, vol. 46, no. 20, pp. 3077–3107, Oct. 1989.
- [38] F. Chen and J. Dudhia, "Coupling an advanced land surface-hydrology model with the penn state-NCAR MM5 modeling system. Part I: Model implementation and sensitivity," *Monthly Weather Rev.*, vol. 129, no. 4, pp. 569–585, 2001.
- [39] K. F. Evans and G. L. Stephens, "Microwave radiative transfer through clouds composed of realistically shaped ice crystals. Part II. Remote sensing of ice clouds," *J. Atmos. Sci.*, vol. 52, no. 11, pp. 2058–2072, Jun. 1995.
- [40] D. Wang *et al.*, "Surface emissivity at microwaves to millimeter waves over polar regions: Parameterization and evaluation with aircraft experiments," *J. Atmos. Ocean. Technol.*, vol. 34, no. 5, pp. 1039–1059, May 2017.
- [41] J. Wang, J. R. A. Houze, J. Fan, S. R. Brodzik, Z. Feng, and J. C. Hardin, "The detection of mesoscale convective systems by the GPM ku-band spaceborne radar," *J. Meteorol. Soc. Jpn.*, vol. 97, no. 6, pp. 1059–1073, 2019.
- [42] E. J. Zipser, D. J. Cecil, C. Liu, S. W. Nesbitt, and D. P. Yorty, "Where are the most intense thunderstorms on Earth," *Bull. Amer. Meteorol. Soc.*, vol. 87, no. 8, pp. 1057–1072, Aug. 2006.
- [43] P. Salio, M. Nicolini, and E. J. Zipser, "Mesoscale convective systems over southeastern south america and their relationship with the south American low-level jet," *Monthly Weather Rev.*, vol. 135, no. 4, pp. 1290–1309, Apr. 2007.
- [44] C. Matsudo and P. Salio, "Severe weather reports and proximity to deep convection over northern argentina," *Atmos. Res.*, vol. 100, no. 4, pp. 523–537, 2011.
- [45] J. P. Mulholland, S. W. Nesbitt, R. J. Trapp, K. L. Rasmussen, and P. V. Salio, "Convective storm life cycle and environments near the sierras de Córdoba, argentina," *Monthly Weather Rev.*, vol. 146, no. 8, pp. 2541–2557, Aug. 2018.

- [46] D. Wang, S. E. Giangrande, Z. Feng, J. C. Hardin, and A. F. Prein, "Updraft and downdraft core size and intensity as revealed by radar wind profilers: MCS observations and idealized model comparisons," *J. Geophys. Res., Atmos.*, vol. 125, no. 11, Jun. 2020, Art. no. e2019JD031774.
- [47] J. Yuan, R. A. Houze, and A. J. Heymsfield, "Vertical structures of anvil clouds of tropical mesoscale convective systems observed by CloudSat," *J. Atmos. Sci.*, vol. 68, no. 8, pp. 1653–1674, Aug. 2011.
- [48] C. Prigent, F. Aires, D. Wang, S. Fox, and C. Harlow, "Sea-surface emissivity parametrization from microwaves to millimetre waves," *Quart. J. Roy. Meteorol. Soc.*, vol. 143, no. 702, pp. 596–605, Jan. 2017.
- [49] M. Klein and A. J. Gasiewski, "Nadir sensitivity of passive millimeter and submillimeter wave channels to clear air temperature and water vapor variations," *J. Geophys. Res., Atmos.*, vol. 105, no. D13, pp. 17481–17511, 2000.
- [50] H. J. Liebe, G. A. Hufford, and T. Manabe, "A model for the complex permittivity of water at frequencies below 1 THz," *Int. J. Infr. Millim. Waves*, vol. 12, no. 7, pp. 659–675, Jul. 1991.
- [51] C. Mätzler, *Thermal Microwave Radiation: Applications for Remote Sensing*. London, U.K.: Institution of Engineering and Technology, 2006.
- [52] J. Fan *et al.*, "Cloud-resolving model intercomparison of an MC3E squall line case: Part I—Convective updrafts," *J. Geophys. Res., Atmos.*, vol. 122, no. 17, pp. 9351–9378, 2017.



Victoria Sol Galligani received the M.Sci. degree in physics from Imperial College London, London, U.K., in 2010, and the Ph.D. degree from the L'École Doctorale d'Astronomie et Astrophysique d'Île-de-France, Paris, France, in 2014.

In 2015, she joined the Centro de Investigaciones del Mar y la Atmósfera (CIMA), Universidad de Buenos Aires (UBA) (Center for Ocean and Atmosphere Research, University of Buenos Aires), Buenos Aires, Argentina. Since 2017, she has been an Assistant Researcher with the Consejo Nacional de Investigaciones Científicas y Técnicas of Argentina (CONICET, the National Scientific and Technical Research Council), CIMA. Her research interests include meteorological remote sensing of the Earth's atmosphere, RT modeling, mesoscale and cloud dynamics, and cloud microphysics.



Die Wang received the Ph.D. degree in physics from the Université Pierre et Marie Curie, Paris, France, in 2016, with a focus on the understanding of scattering processes of cloud ice particles and the retrieval of cloud microphysical properties from satellite microwave remote sensing measurements.

She has been an Assistant Scientist with the Brookhaven National Laboratory, Upton, NY, USA, since 2020. She also serves as the instrument mentor for the rain gauges and disdrometers operated by the U.S. DOE Atmospheric Radiation Measurement

Program. Since coming to Brookhaven National Laboratory, her research interests have been focused primarily on observational studies to better understand the deep convective cloud systems and their insights for the improvement of regional to global climate modeling capabilities.



Paola Belén Corrales received the M.Sci. degree in atmospheric sciences from the Universidad de Buenos Aires, Buenos Aires, Argentina, in 2018. She is pursuing the Ph.D. degree with the Centro de Investigaciones del Mar y la Atmósfera (CIMA), Universidad de Buenos Aires (UBA) (Center for Ocean and Atmosphere Research, University of Buenos Aires).

Her research aims to improve severe weather forecasts at a mesoscale level using data assimilation techniques. She has worked with radar data devel-

oping the *rvad* R package to calculate wind profiles using Doppler velocity and now she is working with satellite radiances to assess their impact on an ensemble assimilation and forecast system.



Catherine Prigent (Member, IEEE) received the Ph.D. degree in physics from Paris University, Paris, France, in 1988.

Since 1990, she has been a Researcher with the Centre National de la Recherche Scientifique (CNRS), Paris Observatory, Paris. From 1995 to 2000, she was on leave from the CNRS and she worked at NASA/Goddard Institute for Space Studies, Columbia University, New York, NY, USA. She is the Co-Founder of Estellus, Paris, a small company specialized in satellite

Earth observations. Her research covers satellite microwave remote sensing of the Earth, for both surface and atmosphere characterization for global applications. It includes RT modeling work (e.g., microwave ocean surface emissivity), retrieval of key surface variables (e.g., microwave land surface temperature, surface water extent, and ocean ice concentration), or the development of cloud estimates from millimeter waves. She is involved in the preparation of several satellite instruments, with ESA, EUMETSAT, and CNES (e.g., MWI and ICI onboard MetOp-SG, the Copernicus CIMR mission, and SWOT).